

Crustal structure and Moho depth profile crossing the central Apennines (Italy) along the N42 degree parallel.

Massimo Di Bona

Francesco Pio Lucente

Nicola Piana Agostinetti

Istituto Nazionale di Geofisica e Vulcanologia, CNT, Rome 00143, Italy

Abstract

We present results from a teleseismic receiver-function study of the crustal structure in the central Apennines (Italy). Data from fifteen stations deployed in a linear transect running along the N42 degree parallel were used for the analysis. A total number of 364 receiver functions were analyzed. The crustal structure has been investigated using the neighborhood algorithm inversion scheme proposed by *Sambridge* [1999a], obtaining crustal thicknesses, bulk crustal V_P/V_S ratio and velocity-depth models. In each inversion, the degree of constraint of the different parameters has been appraised by the Bayesian inference algorithm by *Sambridge* [1999b]. The study region is characterized by crustal complexities and intense tectonic activity (recent volcanism, orogenesis, active extensional processes), and these complexities are reflected in the receiver functions. However, the relatively close spacing among the seismometers (about 20 km) helped us in the reconstruction of the crustal structure and Moho geometry along the transect. Crossing the Apennines from west to east, the Moho depth varies by more than 20 km, going from a relatively shallow depth (around 20 km) on the Tyrrhenian side, deepening down to about 45 km depth beneath the external front of the Apenninic orogen, and rising up again to about 30 km depth in correspondence of the Adriatic foreland. Despite the strong variability of the crustal thickness, the average crustal

V_S values show little variation along the transect, fluctuating around 3 km/s. The average V_P values obtained from the V_S and V_P/V_S are generally lower than 6 km/s.

1. Introduction

Determination of the Earth's crustal structure and Moho geometry and depth is a primary task for geological and geophysical study, as well as a key ingredient to the successful application of many further analyses (from earthquake location, to mantle tomography, to seismic hazard assessment). Over the years seismology has greatly contributed to a better knowledge of the Earth's outer shell, allowing, together with geological, petrological, and geochronological information, to discriminate different primary crustal types [see *Mooney et al.*, 1998, for a review]. However, in complex tectonic environments, the crust rarely falls within one of the primary types, rather being a mixture of types. The Apennines, in Italy, are a manifest example of a complex tectonic environment. They are part of the Mediterranean Alpine belt, and result from the emergence of the accretionary wedge formed during the westward subduction of the Adriatic lithosphere (Figure 1). The Apennines are predominantly formed by a Meso-Cenozoic sedimentary sequence, deformed during late Miocene-Pleistocene time, through eastward frontal accretion of thrust sheets stacked over the Adriatic foreland. The accretion process was synchronous with extension in the internal part of the eastward migrating wedge [*Elter et al.*, 1975; *Patacca et al.*, 1990] and accompanied by diffuse volcanism and emplacement of intrusive bodies in the crust along the Tyrrhenian margin [*Serri*, 1990]. The crustal structure of Italy has been investigated by a number of active seismic experiments [see *Finetti*, 2005 for a review] and most of the information built into the existing crustal models is largely derived from seismic refraction or reflection data that provide accurate estimates of the depth to the Moho and compressional wave velocities (V_P). However, these models suffer from a lack of constraints on shear wave velocities (V_S) in the

crust. Measurement of V_S becomes particularly important in young and active tectonic environments, where the seismic velocities and the chemical aggregates marking the crust-mantle boundary do not necessarily have coinciding depths [Griffin and O'Reilly, 1987]. As a matter of fact, the V_S is more sensitive, hence a better discriminant, in the presence of complex structures (i.e. fluid filled cracks, anisotropy, partial melt) that could display similar V_P values [Christensen, 1996].

Teleseismic receiver functions (RF) are viewed as a primary source of detailed information on the V_S contrasts within the crust and the upper mantle, and have become a standard tool for imaging the Moho and other crustal and mantle discontinuities [e.g. Bostock, 1998; Zhu and Kanamori, 2000; Ramesh et al., 2002; Dugda et al., 2005]. In Italy, the RF technique has been recently used to image the gross crustal structure and thickness across the northern Apennines [Piana Agostinetti et al., 2002; Levin et al., 2002; Mele and Sandvol, 2003]. Although coming from the same data-set, the results obtained by these previous RF studies show some discrepancies which can be attributed to factors inherent both in the different RF modeling approaches, and in the complexity of the crustal structure of the study area. Such discrepancies were not properly assessed, because these studies lack an error estimate on the determined parameters (crustal layer thicknesses, V_P/V_S ratios and velocity-depth models). In a recent paper Mele et al. [2006] determined the crustal thickness across the central Apennines, via RF analysis, from the same dataset used in this study. Here we investigate the crustal structure across the central Apennines applying the neighbourhood algorithm inversion scheme proposed by Sambridge [1999a] to a dataset of 247 selected RFs. We estimate the uncertainty on the results by applying a Bayesian inference algorithm [Sambridge, 1999b]. The similarities and discrepancies between the results obtained in Mele et al. [2006] and in this study will be discussed.

2. Data and RF Computation

The data used in this RF analysis were recorded by the Central Apennines (CAP) seismic transect, deployed in 1995 in the framework of the project GeoModAp [Amato *et al.*, 1998], with the aim of collecting teleseismic recordings for studies of the lithosphere-mantle structure. The seismic array consisted of 15 stations (CANN, with NN=00-14) located along the N42 degree parallel from the Tyrrhenian coast to the Tremiti islands in the Adriatic sea (Figure 1), with an average spacing of about 20 km. Each recording site was equipped with a 24 bit digitizer (RefTek 72A-07) connected to a tri-axial enlarged-band (Lennartz LE-3D/5s) or broad-band (Güralp CMG-4T and CMG-3T) sensor. The data were continuously recorded at 20 samples per second. The lower limit of the frequency band, in which the instrument response is flat to ground velocity, is equal to 0.2, 0.03 and 0.01 Hz, depending on the sensor. The recording campaign lasted four months from April to July.

The relatively short recording period led us to select teleseismic events with $m_b \cong 5$ as the lower magnitude limit and, at first, to discard the corresponding data only when no clear P -wave onset was seen on at least one of the 1 Hz low-pass filtered seismograms on the vertical, NS and EW components of ground motion. Moreover, the events were selected with the epicentral distance ranging from 30 to 100 degree.

Radial and tangential RFs were computed for the initial data collection consisting of 364 tri-axial P -wave seismograms recorded for 65 earthquakes ($5.1 \leq m_b \leq 6.7$). Following Langston [1979], they were obtained by deconvolving the vertical seismogram from the horizontal (radial and tangential) seismograms. The tangential direction is positive at 90 degree clockwise from the radial direction, which is positive away from the source. The deconvolution was performed in the frequency domain by using the method proposed by Oldenburg [1981]. This technique optimally handles the trade-off between resolution and variance through a damping parameter, allowing to incorporate the additive noise which

affects the seismograms and to assess the statistical accuracy of the RFs amplitudes. Following *Di Bona* [1998], this approach is used jointly with a measurement of the power spectral density of the noise which affects the receiver function in the segment preceding the *P* pulse, in order to include the contribution of the signal-generated noise to the estimate of the receiver function variance. The Fourier transforms of the vertical and the horizontal signals were computed for 120 s time windows around the first *P*-wave arrival. Moreover, following *Langston* [1979] and *Ammon* [1991], we applied a Gaussian filter to limit the spectral content to the frequency band below about 1 Hz and a multiplication factor to normalize the averaging functions to unit maximum amplitude in the time domain, respectively.

A visual inspection of the computed RFs proved that their quality was highly variable within this initial set. A considerable number of RFs were excluded from the subsequent analysis, as they were characterized by relatively large amplitudes in the segment preceding the *P*-wave arrival (owing to deconvolution noise or large side-lobes in the averaging function), or had a monochromatic appearance (in spite of the low amplitudes in the pre-signal window) indicating an unstable result of the deconvolution. Therefore, we chose 247 RFs, corresponding to 56 teleseisms listed in Table 1. The distribution of these events in backazimuth and epicentral distance is shown in Figure 2. The selected waveforms are unevenly distributed among the stations: CA01, CA02 and CA10 provided the largest number of RFs (30-39), CA13 did not produce any waveforms useful for the subsequent analysis, and 6-19 RFs were obtained for each of the other sites. Half of the selected RFs have standard deviations which are less than about 11% and 13% of the maximum amplitude in the time window 0 – 6 s for the radial and tangential signals, respectively.

The selected teleseisms provide an uneven coverage in both backazimuth and epicentral distance, as the global seismicity recorded in Italy samples mostly backazimuths in the NE

and NW quadrants and the largest epicentral distances (> 70 degree) in the range useful for RF analysis (usually $30 - 100$ degree), and this effect is heightened for short recording times. However, the stations CA01 and CA02 exhibit an acceptable coverage in both backazimuth and epicentral distance: the selected events sample all four of the backazimuth quadrants and eleven of them have distances less than 70 degree. Most of the other stations have only one radial and tangential receiver function with the backazimuth in the SW quadrant and no receiver function with the backazimuth in the SE quadrant. For all the stations, there is at least one selected teleseism with epicentral distance less than 70 degree.

Stacking of radial and tangential RFs was carried out in order to lower the uncorrelated noise. For each group of RFs selected for stacking, the weighted average was computed at each sample with the weights set to the reciprocal of the RF variances. For some stations (CA01, CA02, CA10, CA11 and CA12), from 5 to 13 RFs with backazimuth and epicentral distance within 30 ± 6 degree and 80 ± 6 degree, respectively, were stacked. In addition, for the stations CA10 and CA12, the RFs selected for stacking include 5 and 4 RFs, respectively, with backazimuth within 63 ± 3 degree and distance within 91 ± 6 degree. Other stacked RFs were computed for CA01, CA02, CA11 and CA14 from groups of fewer RFs in narrower intervals of backazimuth and epicentral distance. The RFs selected for the stations from CA03 to CA09 are characterized by a variability of their radial and tangential components with backazimuth, which appears to be mostly random in nature and possibly caused by noise or by scattered waves generated by complex 3-D heterogeneities in the receiver-side structure. For this reason, we chose to stack the receiver functions from these stations in wider intervals of backazimuth. Two classes of epicentral distances, less or greater than about 70 degree, respectively, were considered; epicentral distances differ from each other by no more than 30 degree in each of these classes, and no significant move-out is expected. In Figure 3 for the station CA01 and in Figures S1-S13 of the electronic supplementary

material, for the other stations, the selected (single event and/or stacked) RFs are shown. In order to evaluate the uncertainty of the stacked receiver functions, we computed their rms values on 10 s long segments from 15 s to 5 s before the direct-P pulse. These estimates were used in place of the standard deviations computed by means of equation (A2), which is valid only for uncorrelated data. In the Appendix, the possible correlation among receiver functions is discussed and the connection between the rms value of the stacked receiver function and the standard deviations of the RFs selected for stacking is empirically established.

3. Inversion Methodology

The *P*-to-*S* converted wave-field emerging from the analyzed RFs is rather complicated for all the sites; the radial RFs are somewhat variable with backazimuth. Moreover, the tangential amplitudes are often comparable to the radial amplitudes. These two circumstances indicate that lateral variations, as well as seismic anisotropy, in the crust and in the upper-mantle are almost ubiquitous beneath the investigated area. The poor quality of some receiver functions and the insufficient azimuthal coverage make it difficult to assess the nature of the 3-D heterogeneities, or to recognize the contribution of possible seismic anisotropy [Levin and Park, 1997, 1998]. For the stations CA01 and CA02, the available azimuthal coverage and the satisfactory quality of most of the RFs allowed us to clearly identify patterns of symmetric and anti-symmetric converted phases versus backazimuth, respectively on the radial and the tangential RFs. We will show that shallow dipping interfaces beneath these stations are required to explain, at least partly, the complexity of the RFs. However the main purpose of our analysis is to extract first-order information about the vertical variation of the seismic velocities in the crust and in the upper-mantle, by modeling the observed RFs through 1-D models. One possible flaw of this approach is that arrivals caused by scattering from lateral heterogeneities may be interpreted as converted phases or reverberations

generated by artificial vertical contrast of the seismic velocities. In order to avoid or to restrict this misinterpretation, when possible, we simultaneously invert RFs for different values of backazimuth or epicentral distance. For each of the stations from CA03 to CA09, a receiver function stack in a wide interval of backazimuths is used for the inversion, in order to get a 1-D approximation to the actual structure. These stacks may be effective in reducing the noise and, by suppressing the arrivals arising from the lateral heterogeneities, enhance the signal produced by the 1-D properties of the structure. Modeling the arrivals common to all the backazimuths may yield information about the laterally homogeneous component of the seismic velocities. In any case, we will not necessarily stress the geological significance of each single feature in the obtained 1-D models, but rather we will emphasize the structural features which are common to multiple sites. Even more emphasis will be placed on some integral quantities (computed from the model parameters), such as the depth of the crust-mantle boundary (the Moho) and the mean crustal velocities of the *P*- and *S*-waves.

The receiver function inversion for a 1-D model of the crust and upper-mantle structure is performed through the two-stage approach proposed by *Sambridge* [1999a, 1999b]. In the first stage, a search method for models with acceptable fit to the data is applied in a multidimensional model space. The search (neighborhood algorithm) is performed by dividing the model space into Voronoi cells, each of these containing one model; the set of Voronoi cells provides an approximation of the misfit surface, in which the misfit value is constant within each cell. An initial set of Voronoi cells is built by generating 1000 random samples (or models), evenly distributed in the feasible region of the model space. Afterwards a given number (N_I) of iterations is executed and, at each iteration, a random walk performed through a Gibbs-sampler produces M new samples (or models), equally distributed in the N_V Voronoi cells enclosing the models with the lowest misfit. The final result is an ensemble of $(1000 + M N_I)$ models, most of them sampling the regions of the model space where the fit to

the data is better. The value of N_V determines the degree of exploration of the model space: for larger values of N_V the algorithm is more exploratory, while a more localized sampling is obtained for smaller values of N_V ; for a fixed value of M , smaller values of N_V also lead to more exploitation as more new models are generated in each cell (for a complete discussion of the influence of the parameters M and N_V , see *Sambridge, 1999a*). In using the neighborhood algorithm, we selected three pairs of values for (M, N_V) in order to sample the model space with a different degree of exploration-exploitation; the number of iterations (N_I) was accordingly chosen so that the total number of models (11000) was the same for all the ensembles. Moreover, for the pair of values for (M, N_V) which corresponds to a sampling with an intermediate degree of exploration, four ensembles are generated by simply using different initial seeds (for the generation of the pseudo-random numbers). Therefore, for each inversion, we obtained six ensembles, the best-fit models of which generally had misfit values that were comparable to each other.

Any measure of data fit goodness can be used in the Sambridge's approach. In this study we chose to weight the contribution of each receiver function according to its noise level, or variance, and we only used a weighted sum of the square residuals as measure of the data fit goodness. Therefore, the misfit function is defined as

$$\chi^2 = \sum_{k,l} \frac{[r_k(t_l) - s_k(t_l)]^2}{\sigma_k^2} \quad (1)$$

where $r_k(t_l)$ is the amplitude at time t_l of the k -th (single event or stacked) receiver function, with σ_k^2 as the estimate of its variance; $s_k(t_l)$ indicates the k -th synthetic receiver function, computed (through the modeling procedure used in *Sambridge [1999a]*) from a 1-D model of the crust and the upper-mantle structure consisting of five homogeneous layers over an half-space. In the misfit computation, the time window of each receiver function begins 5 s before the direct- P arrival and is 35 s long. For most of the stations the receiver functions exhibit

converted phases or reverberations at short times after the direct- P arrival, suggesting that at least one or two very shallow layers are needed to model the initial segment of the receiver functions. For this reason, selecting five layers means that at least three layers are used for the remainder of the crust and the upper-mantle. Note that the inversion procedure allows to obtain models with small or unimportant velocity contrast at some interfaces if, relatively to the noise level in the receiver functions, these models (symbolizing models with less layers) provide a fit to the data which is better than or comparable with the fit from other models with a larger effective number of layers. The model parameters include: the thickness h of each layer, the density ρ , the S -wave velocity V_S , the ratio of P to S velocity (V_P/V_S), and the quality factors Q_P and Q_S for the P - and S -waves, for each layer and for the half-space. Only some of these parameters are allowed to vary (h , V_S , V_P/V_S); therefore, the total number of free parameters, or the dimension of the model space, is equal to 17. Moreover, the following integral parameters are included in the computation: the Moho depth, defined as

$$H = \sum_k h_k \quad (2)$$

where the summation is over the layers which compose the crust; the mean slowness in the crust for the longitudinal and shear waves, defined as

$$\left\langle \frac{1}{V_w} \right\rangle = \frac{\sum_k h_k / V_{wk}}{\sum_k h_k} \quad (3)$$

($w = P, S$); the mean ratio of P to S velocity in the crust, computed as

$$\left\langle \frac{V_P}{V_S} \right\rangle = \frac{\sum_k h_k V_{Pk} / V_{Sk}}{\sum_k h_k} \quad (4)$$

which, like the mean slowness in the equation (3), is a weighted average with the layer thicknesses as weights. As a general rule, we define the Moho as the interface where the S -wave velocity reaches values typical for the sub-crustal mantle (i.e. around 4.5 km/s; see

Kennet et al., 1995 and references therein). In the study of the dipping structures beneath the stations CA01 and CA02, as described below, the synthetic receiver functions were computed through the modeling procedure developed by *Frederiksen and Bostock* [2000]. In this case, the set of the model parameters also includes the strike and the dip angles of each interface, whereas the quality factors for the anelastic attenuation are not considered in the receiver function computation.

As many models in each of the final ensembles have similar values of the misfit, we get a range of solutions, clustered in families of models, which provide comparable fits to the data. The different location of such families within the model space reveals the trade-off among the model parameters (for example, between the seismic velocities and the thickness). In the course of analysis, some of these families were discarded when they provided geologically unreasonable structures. Besides, visual comparison between the observed and the synthetic receiver functions (computed from the best fit model) was performed in order to better evaluate the goodness of the fit to the main arrivals and, if needed, to exclude unsatisfactory models. In fact, for noisy receiver functions some models, when compared to other models with similar values of misfit, may provide a worse fit to arrivals which are judged important to define some elements of the structure, such as the crust-mantle boundary.

The second stage of the Sambridge approach is the appraisal of the ensemble of models generated in the first stage by the neighborhood algorithm. It consists in resampling the model space by using the information provided by the available ensemble of models: the new points sample an appropriate approximation of the posterior probability density, built from the input ensemble of models for which the misfit values have been computed. Within a Bayesian framework, and using multidimensional Monte Carlo integration, from the new resampled ensemble the marginal posterior probability density (MPPD) is computed for each model parameter, or for other quantities defined as functions of the model parameters (such

as, the Moho depth, the mean P - and S -wave slowness in the crust and their ratio, defined through equations 2-4). In this way, we get a measure of uncertainty for the properties of the velocity structure. The joint MPPD for any pair of parameters can also be computed, allowing some inference about the possible trade-off. The prior probability density function, required in the Bayesian analysis, is simply set to be uniform within the allowed region of the model space. This means that the available prior information on the model only allows us to set the boundary of the feasible region in the model space. (For a complete description of the technique, including the resampling algorithm, see *Sambridge, 1999b*.)

In our analysis the appraisal stage was applied to each of the ensembles selected in the first stage: the ensembles with unsatisfactory families of models with (similar) lower misfit were discarded (as previously described). The obtained results (the MPPD functions for each parameter) were compared to each other for consistency. First of all, we judged whether each of the input ensembles appropriately sampled the regions of high data fit. To this end, the requirements to be fulfilled were: (1) the potential scale reduction (PSR) factor was less than 1.2 for all the parameters (following *Sambridge, 1999b*), thus requiring that the resampled ensemble was actually distributed according to the approximate posterior probability density; (2) the parameters of the best fit model were reasonably close to the maximum of their MPPD functions (relatively to the width of the latter). After the exclusion of the poor quality ensembles, the results obtained from the remaining ensembles proved to be reasonably consistent for most of the model parameters; greater accord was achieved for the integral parameters, such as the Moho depth, the mean P - and S -wave slowness in the crust and their ratio (equations 2-4), which were also characterized by less uncertainty.

The bounds of the model parameters allowed to vary were generally different from station to station, in order to increase the sampling density in those regions of the model space where the models produce synthetic receiver functions more similar to the observed ones. For each

station, the bounds of the model parameters were selected through forward modeling. Table 2 summarizes the values of the fixed parameters together with the general bounds for the model parameters allowed to vary; for each station the actual bounds fall into the ranges specified in this table.

4. RF analysis and inversion results across the CAP transect

As previously described, the inversion approach consists in outlining the features which characterize the class of 1-D models with a similar fit to the data. The appraisal stage provides estimates of the variability, or uncertainty, for the corresponding determinations of the crustal thickness and of the mean seismic velocities, which are the primary outcomes we consider in this study.

At each station, the radial receiver functions for different backazimuths have a degree of similarity in the first few seconds which is variable from station to station. In some cases, similar features in the radial receiver functions are observed in a wide range of backazimuth, whereas a larger variability is observed in other cases. Possible P_s converted phases generated by the Moho can be recognized along the transect at times ranging from 3 to 6 s after the direct- P arrival. In particular, for station CA02, this arrival is slightly delayed in some receiver functions for approaches from the northeast, suggesting a variable depth of the Moho beneath this station.

For some stations the first pulse in the radial receiver function is wide and slightly delayed with respect to the direct- P arrival; both of these features may be the effects of low velocity layers in the near-surface structure. An observation common to more stations is the variation with the backazimuth of the shape and the timing of the first pulse, which we name apparent direct- P arrival following *Darbyshire* [2003]. The time delay and the variability of the first pulse is caused by interference between the true direct- P pulse and a P_s phase (and/or a

reverberation) from a shallow, possibly dipping [Owens and Crosson, 1988], interface with an high velocity contrast.

In the following we describe the analysis of the RF data at station CA01, which enjoys azimuthal coverage that is among the best of our set. The details concerning the RFs selection for the inversion, the fit to the data and the 1-D models obtained for the other stations are illustrated in the text of the electronic supplementary material and in the Figures S1-S13.

For station CA01, receiver functions are available in all four backazimuth quadrants. Radial and tangential RFs have similar amplitudes, and patterns of pulses with polarity reversals are evident within the first 2 seconds of the direct-*P* arrival (Figure 3a,b). Patterns of anti-symmetric and symmetric *P*-to-*S* converted phases versus the backazimuth, respectively on the tangential and the radial RFs, can be interpreted as originating from a dipping interface [Langston, 1977; Owens and Crosson, 1988]. An alternative explanation is the presence of seismic anisotropy in the crust and upper-mantle [Levin and Park, 1997, 1998]. For the tangential RFs of station CA01, polarity reverses two times: around N65E and between N224E and N266E (Figure 3b). The polarity distribution would be consistent with a near-surface interface dipping approximately N65E (where the tangential amplitudes are the lowest) or, equivalently, with a strike direction of about N25W. On the radial component, the first 1.5 seconds of the receiver functions are characterized by the interference between the direct-*P* and the *P*_s phases generated by the shallow dipping interface (Figure 3a). Moving away from the up-dip direction, at first the direct-*P* pulse is absent (or slightly negative) and the *P*_s arrival has a large positive amplitude, producing a shifted apparent direct-*P* arrival (Figure 3a). Beyond the strike direction, the direct-*P* pulse has relatively large amplitude while the amplitude of the *P*_s pulse becomes low (or negative) close to the down-dip direction. The large range in backazimuth (at least 100 degrees) in which the *P*_s phase dominates and the change of polarity for the mix of the direct-*P* and the *P*_s phases suggests

that the dip angle of the interface is relatively high [Owens and Crosson, 1988]. In the interpretation of the RFs of the station CA01, we have ruled out seismic anisotropy as the main cause; the nearly zero (or slightly negative) direct- P pulse on the radial component would require unreasonably high percentage (40% or more) of seismic anisotropy, as demonstrated by *Lucente et al.* [2005].

In order to constrain the geometry of the dipping interface beneath CA01, the inversion procedure was applied to short segments of the (25) radial and tangential (single-event or stacked) RFs, for a model consisting of one layer over a halfspace separated by a dipping interface. In the misfit computation, the time window of each receiver function begins 2.5 s before the direct- P arrival and is 5 s long (gray area in Figure 3a,b). In addition to the parameters described above for the 1-D model, the strike and the dip angles of the interface are allowed to vary (Table 3), whereas the quality factors for the anelastic attenuation are not included. The range of strike directions of the interface was selected so as to include the strike direction (N25W) inferred from the initial analysis of the receiver functions. Synthetic receiver functions for the dipping structure were computed through the modeling procedure developed by *Frederiksen and Bostock* [2000] (red traces in Figure 3a,b). Each of the ensembles of models generated by the inversion procedure was characterized by a best-fit model with the strike and the dip angles equal to 340-341 degree and 45-46 degree, respectively (strike 340 degree and dip 45 degree are shown in the azimuthal plot inset in Figure 3c), with the V_P/V_S ratio equal to 2.06 in the first layer, and with the other parameters varying in narrow ranges. A further inversion was carried out in order to determine a 1-D model of the structure below the dipping interface. We considered models consisting of one surface layer with a dipping interface and four horizontal layers overlying the half-space. The strike and the dip angles of the shallow interface and the V_P/V_S ratio (in the first layer) are fixed and equal to the best-fit values obtained in the first inversion (340 degree, 45 degree

and 2.06, respectively). The thickness and the S -wave velocity in the first layer are allowed to vary within the ranges obtained for the family of models produced by the first inversion (1.5 – 1.8 km and 1.0 – 1.2 km/s, respectively). The values of the density and the ranges of variability for the layers thickness, and the V_S and the V_P/V_S ratio in the other layers and in the halfspace are shown in Table 2. The four (stacked or single-event) receiver functions used for this inversion were selected according to the quality of the signals and so that different epicentral distances were sampled; moreover, we inverted RFs for different values of backazimuth in order to get the best 1-D approximation of the velocity structure below the dipping interface. These RFs are shown as thicker traces in Figure 3a and compared to their respective synthetics in Figure 3d.

The final model (shown in Figure 3c) is characterized by relatively low seismic velocities. In the two shallowest layers (thicknesses 1.6 and 3.7 km, respectively) the V_S values are 1.0 and 2.3 km/s, respectively. At greater depth, the S -wave velocity increases but its maximum value (3.9 km/s at about 20 km in depth) is significantly smaller than the values (around 4.5 km/s) typical for the mantle rocks. On average, the values of V_S , V_P and V_P/V_S in the crust (excluding the shallow layer) are 2.8 km/s, 4.8 km/s and 1.73, respectively. The overall low seismic velocities may be consistent with the volcanic nature of the area where the station CA01 is located. Furthermore, the relatively recent volcanic activity in this region (from the lower up to the middle Pleistocene, see *Karner et al.*, 2001) may explain the lack of a clear signature of the crust-mantle boundary. Instead, if the layer with the highest seismic velocities was interpreted to be the upper mantle (conjecturing an underestimation of the seismic velocities in the deeper part of the model), an estimate of the Moho depth equal to 20 km would result. In the first 5 seconds from the direct- P arrival, there is a satisfactory agreement between the synthetic and the observed RFs (Figure 3d); the features in the first 1.5 second of the receiver functions are produced by the dipping boundary of the shallow

layer. The P_s phase generated by the supposed Moho arrives at about 3.5 s after the direct- P arrival and is stronger for western backazimuths and smaller epicentral distances. No significant arrival produced by the deepest interface is evident on both the synthetic and the observed RFs (outside the noise level); the velocity contrast at this interface is relatively low for both the P - and the S -wave, and a 1-D model without this interface may provide a comparable fit to the receiver functions, relatively to the noise level.

For station CA02, receiver functions are available in all four backazimuth quadrants and are shown in Figure S2a,b (in the electronic supplementary material). The presence of tangential ground motion characterized by two polarity reversals can be explained by a dipping structure and its pattern versus backazimuth suggests similar directions for the dipping interfaces. The radial receiver functions exhibit an apparent direct- P that is shifted for all the backazimuth values, and this shift is larger for approaches from the southwest and the northwest. This behavior can be explained by a near-surface layer with very low S -wave velocity and bounded below by an interface dipping due NE, which separates it from a deeper layer with an interface dipping in the SW direction at a relatively higher angle. Accordingly, a preliminary inversion of the radial and tangential RFs for a model consisting of two layers over an half-space, each of these layers bounded below by a dipping interface, and the two interfaces dipping in opposite directions (as previously stated), was run. The result obtained in the first inversion for the shallow dipping structure was incorporated in a further inversion carried out to determine a 1-D model for the deeper (crust and mantle) structure (details can be found in the electronic supplementary material).

For the other stations, inversions of radial (stacked or single-event) receiver functions were performed for 1-D models of the crust and upper-mantle structure. In particular, for stations CA02 and CA11, two groups of receiver functions with different ranges of backazimuth (NE and SW-NW) were inverted separately. The comparison between the synthetic and the

observed traces, for a representative receiver function of each station, is shown in Figure 4. The match between the synthetic and the observed receiver functions is satisfactory for the P_s phase and/or $PpPs$ multiple generated by the Moho at most of the stations. An interface within the upper mantle, and associated with a velocity inversion, is evidenced by a P_s arrival with negative polarity for stations CA00, CA02 and CA03, on the westernmost side of the transect. The 1-D models of the crust and upper-mantle structure along the transect are displayed in Figure 5. The MPPD functions obtained through the appraisal stage for the Moho depths and the average seismic velocities and V_p/V_s in the crust are shown in Figure 6. For stations CA02 and CA11, two 1-D models are obtained (Figure 5), and represent the crust and the upper-mantle structure on the eastern and western sides, respectively. In the models for CA02, the crustal thickness differs by about 5 km, the Moho being deeper on the eastern side. For station CA11, the typical velocity values of the upper mantle are reached at depths which differ by about 10 km, on the eastern and western sides; the two discontinuities are hard to interpret as the same crust-mantle boundary.

For station CA01, below which a clear transition to the typical velocity values of the upper mantle is not found, the depth at which the largest seismic velocity is reached (taken as a trial estimate of the Moho depth) would be consistent with the Moho depth (24 km) beneath station CA00, about 30 km apart from station CA01. The two stations have also a similar trend of S-wave velocity with depth (Figure 5).

Problems with the modeling (described in the electronic supplementary material) of the upper-crustal structure beneath CA09 yields an uncertain estimate of the Moho depth, as confirmed by the corresponding MPPD function shown in Figure 6.

In the following, we restrict our interpretations to the Moho depth, to the average seismic velocities, and to some features in the crust and the upper-mantle which appears to be correlated within groups of neighboring stations.

5. Discussion

We summarize the results of our analysis both in terms of velocity-depth models beneath the seismic stations (Figure 5) and in terms of variation of Moho depth (H), average S - and P -wave crustal velocity (V_S and V_P), and crustal V_P/V_S along the transect (Figure 6). These quantities are represented together with their MPPD, allowing for an immediate estimate of uncertainties associated to these properties (Figure 6). In these figures the two stations CA02 and CA11 have velocity-depth models -and H, V_S and V_P/V_S estimates- on both the eastern and western sides (CA02-E and -W, CA11-E and -W, respectively).

Almost all the computed S -wave velocity models are characterized by very low-velocity uppermost structure, as low as 1.0 km/s at some stations (Figure 5). These low values are interpreted to be related to the presence at surface of either unconsolidated sediments in the Pleistocene basins or weathered exposed rocks. When the number and the azimuthal distribution of the RFs were suitable for 3-D modeling (at CA01 and CA02), the analysis provided evidence for the presence of dipping shallow structures. For example, below CA02, the RF analysis suggests the presence of two inclined layers at shallow depth, dipping in roughly opposite directions, forming a wedge-like structure in the uppermost crust. The geometry of the deeper interface (dip angle = 34 degree) appears consistent with the available geological information about the thrust structure of the Mount Soratte area, where the station CA02 is located [*Servizio Geologico Nazionale*, 1961]. The eastward deepening (with 16 degree angle) thin, low-velocity layer at the top ($h = 0.6$ km, $V_S = 1.1$ km/s) is in agreement with the presence of Plio-Pleistocenic sediments on the west flank of Tiber valley [*Servizio Geologico Nazionale*, 1961].

Looking at the crustal part of the velocity profiles (Figure 5), these can be grouped in two main classes: in the first velocity monotonically increases with depth, the second is

characterized by the presence of velocity inversions within the crust. Apart from CA00, on the westernmost side, all the stations displaying such velocity inversion (from CA06 to CA11) are located over the Apennines mountain range (Figure 5). Inversions in velocity profiles can be explained by the architecture of the Apennines, which were formed through accretion of stacked thrust sheets [Elter *et al.*, 1975; Patacca *et al.*, 1990], producing inverted stratigraphic sequences. In all the shown *S*-wave velocity models, belonging to 14 of the 15 stations along the transect, it is possible to identify the crust-mantle transition, which is generally represented by a sharp discontinuity, where the *S*-wave velocity reaches values typical for the sub-crustal mantle (Figure 5). A further noteworthy feature is the presence at some stations of an interface within the sub-crustal mantle, with a relatively low velocity layer below (Figure 5). This characteristic is more pronounced at some of the westernmost stations (CA00, CA02 and CA03) where velocity decreases down to roughly 4.0 km/s. The *S*-wave low-velocity region found in the uppermost mantle on the Tyrrhenian side (light red area in Figure 5) corresponds to the *P*-wave slow anomalies imaged by tomography [Lucente, *et al.*, 1999; Wortel and Spakman, 2000; Piromallo and Morelli, 2003] and is in good agreement with the observed high heat flow and the presence of quaternary volcanoes in the peri-Tyrrhenian area [Serri 1990; Serri *et al.*, 1993], advocating a deep origin of these thermal anomalies related to the westward subduction process which originates the Apennines.

Going into a more detailed analysis, we concentrate on four main properties of the crust: the crustal thickness (Moho depth), the mean V_S , the bulk crustal V_P/V_S ratio, and the mean V_P . The variation of these quantities along the transect is represented in Figure 6. For almost the totality of the estimates of these four parameters, the best-fit values are close to the maxima of the MPPD distributions (Figure 6).

Receiver functions constrain shear velocity contrasts at interfaces by modeling the pulse amplitude, and only the relative travel-times of the converted and reverberated waves can be measured, so that a depth-velocity trade-off exists [Ammon *et al.*, 1990]. In order to remove this inherent non-uniqueness, the averages of the seismic velocities computed from the inversion results should be matched to those derived from independent studies, which use more appropriate methods for the velocity estimation. Therefore, combining the estimates of mean V_S and V_P/V_S in the crust we evaluate the mean crustal P -wave velocity at each station, in order to compare them with existing information in the study area, which, to our knowledge, is only available from tomographic studies [Di Stefano *et al.*, 1999].

The mean crustal V_S we determine is close to 3.0 km/s for most of the stations, except for three stations (CA00, CA07, and CA12), where the mean shear velocities are ~ 3.6 km/s. The lowermost values (2.8 km/s) are found at stations CA01 and CA02, which are located inside and at the margin of the *Roman Magmatic Province*, respectively [Servizio Geologico Nazionale, 1961].

The crustal V_P/V_S ratio along the transect spans between 1.69 and 1.75 (Figure 6), except for stations CA00, CA03, CA07, CA10 and CA12, for which it reaches higher values (up to 1.85 at CA07). Our computation produces very low crustal mean V_P values, as low as 5.0 km/s at most of the sites, while relatively higher V_P values are found only in association with larger values of V_P/V_S (Figure 6). Compared with an extensive compilation of the main crustal characteristics in different continental tectonic environments [Mooney *et al.*, 1998], the V_P values we obtain for the crust across the central Apennines fall close to the lower edge of the range of variation displayed by the various statistical populations. However, low P -wave velocity values are mainly represented in the statistics belonging to Arc and Fore-arc tectonic provinces, which are likely the most appropriate settings among those reported by Mooney *et al.* (1998), the Apennines being the emerged accretionary wedge formed during the westward

subduction of the Adriatic lithosphere. Furthermore the low velocities we determined for the crust in the Apennines region are fairly consistent with tomographic imaging [Di Stefano *et al.*, 1999], which indicates the presence of a low-velocity belt beneath the Apennines, with V_P values by far lower than 6.0 km/s, corresponding to the central part of the orogen.

Looking at the crustal thickness from west to east we observe a general deepening of the Moho, which goes from 20-25 km, on the Tyrrhenian side, down to more than 40 km depth, under the external front of the chain, and then rising again up to about 30 km beneath the Adriatic foreland (cfr. Figure 5 and Figure 6). More in detail, the crust-mantle boundary exhibits a stair-step trend. From CA00 to CA02-W the Moho is confined within the first 25 km depth; these stations lie on the Tyrrhenian margin, which underwent extension, crustal thinning and volcanic activity, and is characterized by high heat flow [Jolivet *et al.*, 1994]. From CA02-E to CA05, the Moho is found at about 30 km depth; at the surface, this sector corresponds to the gentle up-sloping internal front of the Apennines (Figures 5, 6). A further sudden change in the crustal thickness occurs between stations CA05 and CA06, where Moho reaches 37 km depth, remaining almost unchanged up to CA08; these stations are located over the highest part of the Apennines range (Figures 5, 6), and the thickening of the crust from 30 to 37 km can be interpreted as the presence of crustal roots, contributing to support the mountain topography. In the segment between the stations CA09 and CA12, on the external front of the Apennines, the Moho geometry is irregular: below CA09 the Moho reaches 41 km depth, but displaying a large uncertainty (broadest MPPD function in Figure 6); in the velocity-depth model determined for CA10, S -wave velocity typical for the mantle (4.4 km/s) marks a discontinuity at about 30 km depth, however a deeper interface is present at 43 km depth, characterized by a further V_S increase; the RF analysis at station CA11 gives two estimates of the Moho depth, which differ by more than 10 km depending on the backazimuth, being 31 km on the east side and 43 km on the west side; the Moho at station

CA12 is 42 km depth (Figures 5, 6). The very steep Moho offsets over quite short horizontal length scale between stations CA09 and CA12 are difficult to interpret, and may partially result from the uncertain identification of the crust-mantle boundary, in an area where high structural complexities are likely present. A possible explanation is based on the fact that, in this area, the crust is doubled by the presence of the under-thrust Adriatic plate, and receiver functions at some stations (e.g., CA10 and CA11) image both Mohos. The easternmost station of the transect, CA14, is located well-inside the Adriatic foreland and there the Moho shallows to about 30 km depth (Figures 5, 6).

Crustal thickness estimates along the same transect of stations were recently obtained through RF modeling by *Mele et al.* [2006], showing, in some cases, results quite different with respect to those obtained in the present study (see Table 4). The Moho depths are similar both on the Tyrrhenian (from CA00 to CA04) and on the Adriatic sides (CA12, CA14) of the transect, where crustal structures imaged by the velocity-depth models are simpler (Figure 5). In contrast, estimates of crustal thickness present values considerably different, as much as 10 km, beneath the bulk of the Apennines orogen (stations CA05-CA07) and on its external front (CA10, CA11), where crustal structure is complicated as an effect of the vertical repetition of sedimentary sequences and possibly of the doubling of the crust. Since the two studies (*Mele et al.*, 2006 and the present study) use the same set of data for the RF computation, the discrepancies in the results are mainly attributable to the different modeling approach adopted. In the present study the seismic velocities are estimated in the RF modeling procedure, while in the paper by *Mele et al.* [2006], the crustal V_P and the Poisson's ratio are assumed a-priori to be 6.3 km/s (stations CA00-CA02) or 6.5 km/s (CA03-CA14) and 0.25 (corresponding to $V_P/V_S = 1.73$) respectively. The combination of these values results in a crustal V_S equal to 3.64 (CA00-CA02) or 3.76 (CA03-CA14), which is by far higher than the mean crustal V_S values we obtained at most of the stations. However,

independent estimates of crustal seismic velocities in this area from tomography [*Di Stefano et al.*, 1999], corroborate the existence of low V_P values in the study region, lower than most common crustal velocities.

6. Summary

We have determined the crustal structure across the central Apennines orogen through receiver function modeling at 14 sites along a seismic transect lying on the N42 degree parallel. In this area, the crust displays an high variability both in thickness and seismic velocity. On the westernmost part of the transect, velocity-depth models are relatively simple with monotonically increasing velocity with depth, shallow crust-mantle boundary at about 20-25 km depth, and a velocity inversion in the mantle about 10 km below the Moho. Going toward east, the Moho becomes progressively deeper and the structure of the crust is characterized by an increasing complexity. The Moho reaches its maximum depth, at more than 40 km, beneath the external front of the Apennines, where the outermost sheets thrust over the Adriatic lithosphere and the presence of crustal doubling can be hypothesized. At the easternmost site of the transect, on the Adriatic foreland, the crust-mantle boundary raises again to about 30 km depth. The generally low values estimated for the seismic velocities are characteristic of young active tectonic environment, mainly represented in the statistical populations descriptive of the Arc and Fore-arc tectonic types [*Mooney et al.*, 1998], consistently with the nature and the time of the formation of the Apennines.

Acknowledgements

We thank Malcolm Sambridge and Andrew Frederiksen for their codes. This study has been performed in the framework of GeoModAp project, contract EV5V-CT94-0464. We also thank the Associate Editor, Frederik Simons, and two anonymous reviewers for their

constructive remarks. We used the GMT software [*Wessel and Smith, 1998*] and the SAC code [*Goldstein et al., 2003*] for the data visualization.

References

Amato, A., L. Margheriti, R. Azzara, A. Basili, C. Chiarabba, M.G. Ciaccio, G.B. Cimini, M. Di Bona, A. Frepoli, F.P. Lucente, C. Nostro, and G. Selvaggi (1998), Passive seismology and deep structure in central Italy, *Pure Appl. Geophys.*, *151*, 479–493.

Ammon, C.J., G.E. Randall, and G. Zandt (1990), On the nonuniqueness of receiver function inversions, *J. Geophys. Res.*, *95*, 15303–15318.

Ammon, C.J. (1991), The isolation of receiver effects from teleseismic *P* waveforms, *Bull. Seism. Soc. Am.*, *81*, 2504-2510.

Bostock, M.G. (1998), Mantle stratigraphy and evolution of the Slave province, *J. Geophys. Res.*, *103*, 21,183–21,200.

Christensen, N.I. (1996), Poisson's ratio and crustal seismology, *J. Geophys. Res.*, *101*, 3139–3156.

Cimini, G.B., and A. Marchetti (2006), Deep structure of peninsular Italy from seismic tomography and subcrustal seismicity, *Ann. Geophys.*, *49* (1), 331-345.

Darbyshire, F. A. (2003), Crustal structure across the Canadian High Arctic region from teleseismic receiver function analysis, *Geophys. J. Int.*, *152*, 372-391.

Di Bona, M. (1998), Variance estimate in frequency-domain deconvolution for teleseismic receiver function computation, *Geophys. J. Int.*, *134*, 634-646.

Di Stefano, R., C. Chiarabba, F.P. Lucente, and A. Amato (1999), Crustal and uppermost mantle structure in Italy from the inversion of *P*-wave arrival times: geodynamic implications, *Geophys. J. Int.*, *139*, 483–498, doi:10.1046/j.1365-246x.1999.00952.x.

Dugda, M. T., A. A. Nyblade, J. Julia, C. A. Langston, C. J. Ammon, and S. Simiyu (2005), Crustal structure in Ethiopia and Kenya from receiver function analysis: Implications for rift development in eastern Africa, *J. Geophys. Res.*, *110*, B01303, doi:10.1029/2004JB003065.

Elter, P., G. Giglia, M. Tongiorgi, and L. Trevisan (1975), Tensional and compressional areas in recent (Tortonian to Present) evolution of north Apennines, *Boll. Geofis. Teor. Appl.*, *17*, 3–18.

Finetti, I.R. (2005), CROP Project, 1: Deep Seismic Exploration of the Central Mediterranean and Italy, edited by I.R. Finetti, *Atlases in Geoscience*, Elsevier.

Frederiksen, A.W., and M.G. Bostock (2000), Modelling teleseismic waves in dipping anisotropic structures, *Geophys. J. Int.*, *141*, 401-412.

Goldstein, P., D. Dodge, M. Firpo, and L. Minner (2003), SAC2000: Signal processing and analysis tools for seismologists and engineers, Invited contribution to "The IASPEI International Handbook of Earthquake and Engineering Seismology", edited by WHK Lee, H. Kanamori, P.C. Jennings, and C. Kisslinger, *Academic Press*, London.

Griffin, W.L., and S.Y.O'Reilly (1987), Is the continental Moho the crust–mantle boundary?, *Geology*, *15*, 241–244.

Jolivet, L., J.M. Daniel, C. Truffert, and B. Goff (1994), Exhumation of deep crustal metamorphic rocks and crustal extension in arc and back-arc regions, *Lithos*, *33*, 3 – 30.

Karner, D.B., F. Marra, and P.R. Renne (2001), The history of the Monti Sabatini and Alban Hills volcanoes: groundwork for assessing volcanic-tectonic hazards for Rome, *J. Volcanol. Geotherm. Res.*, *107*, 185-219.

Kennett, B.L.N., E.R. Engdahl, and R. Buland (1995), Constraints on seismic velocities in the Earth from traveltimes, *Geophys. J. Int.*, *122*, 108-124.

Langston, C.A. (1977), The effect of planar dipping structure on source and receiver responses for constant ray parameter, *Bull. Seism. Soc. Am.*, *67*, 1029-1050.

Langston, C. A. (1979), Structure under Mount Rainier, Washington, inferred from teleseismic body waves, *J. Geophys. Res.*, *84*, 4749–4762.

Levin, V., and J. Park (1997), Crustal anisotropy in the Ural mountains foredeep from teleseismic receiver functions, *Geophys. Res. Lett.*, *24*, 1283– 1286.

Levin, V., and J. Park (1998), P–SH Conversions in layered media with hexagonally symmetric anisotropy: a cookbook, *Pure appl. Geophys.*, *151*, 669–697.

Levin, V. , L. Margheriti, J. Park, and A. Amato (2002), Anisotropic seismic structure of the lithosphere beneath the Adriatic coast of Italy constrained with mode-converted body waves, *Geophys. Res. Lett.*, 29, 15-18.

Lucente, F.P., C. Chiarabba, G.B. Cimini, and D. Giardini (1999), Tomographic constraints on the geodynamic evolution of the Italian region, *J. Geophys. Res.*, 104, 20,307-20,327.

Lucente, F.P., N. Piana Agostinetti, M. Moro, G. Selvaggi, and M. Di Bona (2005), Possible fault plane in a seismic gap area of the southern Apennines (Italy) revealed by receiver function analysis, *J. Geophys. Res.*, 110, B04307, doi:10.1029/2004JB003187.

Mele, G., and E. Sandvol (2003), Deep crustal roots beneath the northern Apennines inferred from teleseismic receiver functions, *Earth Planet. Sci. Lett.*, 211, 69-78.

Mele, G., E. Sandvol, and G.P. Cavinato (2006), Evidence of crustal thickening beneath the central Apennines (Italy) from teleseismic receiver functions, *Earth Planet. Sci. Lett.*, 249, 425–435.

Mooney, W.D., G. Laske, and T. Guy Masters (1998), CRUST 5.1: A global crustal model at $5^{\circ} \times 5^{\circ}$, *J. Geophys. Res.*, 103, 727–748.

Oldenburg, D.W. (1981), A comprehensive solution to the linear deconvolution problem, *Geophys. J. R. Astron. Soc.*, 65, 331-357.

Owens, T.J., and R.S. Crosson (1988), Shallow structure effects on broadband teleseismic P waveforms, *Bull. Seism. Soc. Am.*, 78, 96-108.

Patacca, E., R. Sartori, and P. Scandone (1990), Tyrrhenian Basin and Apenninic Arcs: kinematic relations since late Tortonian times, *Mem. Soc. Geol. It.*, 45, 425–451.

Piana Agostinetti, N., F.P. Lucente, G. Selvaggi, and M. Di Bona (2002), Crustal Structure and Moho Geometry beneath the Northern Apennines (Italy), *Geophys. Res. Lett.*, 29, 1999, doi:10.1029/2002gl015109.

Piomallo, C., and A. Morelli (2003), P wave tomography of the mantle under the Alpine-Mediterranean area, *J. Geophys. Res.*, 108, 2065, doi:2010.1029/2002JB001757.

Ramesh, D.S., R. Kind, and X. Yuan (2002), Receiver function analysis of the North American crust and upper mantle, *Geophys. J. Int.*, 150, 91–108.

Sambridge, M. (1999a), Geophysical inversion with a neighbourhood algorithm-I. Searching a parameter space, *Geophys. J. Int.*, 138, 479–494.

Sambridge, M. (1999b), Geophysical inversion with a neighbourhood algorithm-II. Appraising the ensemble, *Geophys. J. Int.*, 138, 727–746.

Serri, G. (1990), Neogene-Quaternary magmatism of the Tyrrhenian region: Characterization of the magma sources and geodynamic implications, *Mem. Soc. Geol. It.*, 41, 219–242.

Serri, G., F. Innocenti, and P. Manetti (1993), Geochemical and petrological evidence of the subduction of delaminated Adriatic continental lithosphere in the genesis of the Neogene-Quaternary magmatism of central Italy, *Tectonophysics*, 223, 117–147.

Servizio Geologico Nazionale (1961), Foglio Geologico n. 144 – Palombara Sabina. *Poligrafico di Stato*, Rome.

Wessel, P., and W.H.F. Smith (1998), New version of the Generic Mapping Tools released, *Eos Trans. AGU*, 79, 579.

Wortel, M.J.R., and W. Spakman (2000), Subduction and slab detachment in the Mediterranean-Carpathian region, *Science*, 290, 1910–1917.

Zhu, L., and H. Kanamori (2000), Moho depth variation in southern California from teleseismic receiver functions, *J. Geophys. Res.*, 105, 2969–2980.

Appendix

Generally, given a set $\{r_k\}$ of N uncorrelated gaussian data with the same expected value μ but different variances $\{\sigma_k^2\}$, the maximum likelihood (and unbiased) estimator of μ is the weighted average

$$\langle r \rangle = \frac{\sum_k r_k / \sigma_k^2}{\sum_k 1 / \sigma_k^2} \quad (\text{A1})$$

In this case, the variance of the estimator $\langle r \rangle$ is given by

$$\sigma_u^2 = \frac{1}{\sum_k 1 / \sigma_k^2} \quad (\text{A2})$$

According to the previous equation, the variance of $\langle r \rangle$ is lower than all the data variances $\{\sigma_k^2\}$, meaning that the average operator defined in equation (A1) lowers the uncorrelated noise in the data. In the RF analysis, we applied the weighted average at each sample of the receiver functions selected for stacking.

The noise affecting a receiver function consists of two parts (ε_1 and ε_2), uncorrelated between them: the former is generated by the additive noise in the original seismograms and is expected to decrease with the increasing magnitude of the events and can be considered uncorrelated among different receiver functions; the latter is the consequence of the approximate convolution model which relates the horizontal seismograms to the vertical one, and behaves like signal-generated noise, independent of the event magnitude [Di Bona, 1998]. The component ε_2 of the noise is expected to be almost the same for a RF set corresponding to teleseisms with backazimuths and epicentral distances in relatively small ranges. This implies that the covariance for each pair of receiver functions equals the variance of ε_2 ($\sigma_c^2 \leq \sigma_k^2$). Because of the partially correlated noise affecting the receiver functions, using equation (A2) underestimates the variance of the stacked receiver function.

When the N data $\{r_k\}$ are correlated to each other, the variance of $\langle r \rangle$ is given by

$$\sigma^2 = \sigma_u^2 \left(1 + \sigma_u^2 \frac{\sum_{k \neq l} C_{kl}}{\sigma_k^2 \sigma_l^2} \right) \quad (\text{A3})$$

where C is the data covariance matrix. For a RF set corresponding to events with backazimuths and epicentral distances in small ranges, the off-diagonal elements of C are all equal to σ_c^2 and the equation (A3) becomes

$$\sigma^2 = \sigma_c^2 + \sigma_u^2 \left(1 - \sigma_u^2 \sigma_c^2 \sum_k \frac{1}{\sigma_k^4} \right) \quad (\text{A4})$$

In order to apply the previous equation, for each RF stacking with similar backazimuths and epicentral distances, we empirically determine σ_c^2 by setting

$$\sigma_c^2 = \min_k \sigma_k^2 \quad (\text{A5})$$

where $\{\sigma_k^2\}$ are the RF variances. This is based on the assumption that the component ε_1 of the receiver function noise can be neglected for the receiver function with the lowest variance, and for an event with sufficiently large magnitude. By using the equation (A5), the equation (A4) yields

$$\sigma^2 \cong \min_k \sigma_k^2 \quad (\text{A6})$$

When a RF set, selected for stacking, corresponds to events with backazimuth and epicentral distance in relatively wide ranges, the component ε_2 of the noise is different (and uncorrelated) for pairs of receiver functions for which backazimuth or epicentral distance are sufficiently different; as a consequence, the corresponding off-diagonal elements of the data covariance C are nearly zero. This suggests that the variance of the stacked receiver function is greater than σ_u^2 (and less than $\min \sigma_k^2$) by an amount which depends on the backazimuth and distance distributions.

As an alternative estimate of the uncertainty for a stacked receiver function, we computed its rms value for a 10 s long segment from 15 s to 5 s before the direct- P pulse. In Figure A1 (panel a), the standard deviation of the radial RFs selected for stacking (in small ranges of backazimuth and epicentral distance, 25-36 degree and 75-86 degree respectively) are plotted versus the events magnitude, for the station CA10; the lines indicate, for the stacked receiver function, the rms value and the estimates of σ_u and σ (the latter computed from the equation A4, with σ_c^2 given by the equation A5). This figure shows that the standard deviations tend to decrease for increasing magnitudes, revealing the decreasing contribution of ε_1 to the receiver function noise in a situation in which the component ε_2 is approximately the same. The rms value is sensibly larger than the estimate of σ_u and approximates the value of σ . In Figure A1 (panel b), the standard deviations of the radial RFs selected for stacking (in wide ranges of backazimuth and epicentral distance, N73W – N75E and 73-98 degree respectively) are plotted versus the events magnitude, for the station CA03; the estimate of σ_u and the rms value for the stacked receiver function are indicated by the two lines. The whole set of standard deviations shows little dependence on the event magnitude, unless a subset of receiver functions with less variable backazimuth and distance, thus sharing the same component ε_2 of the noise, is considered. The rms value is slightly greater than the estimate of σ_u and less than the minimum standard deviation within the RF set.

Figure A1 (panel c) shows the values of the standard deviation σ versus the rms values, for the stacked (radial) receiver functions. As a comparison, this figure also displays the standard deviation of each radial receiver function versus the rms value computed in a segment which ends 5 s before the direct- P pulse. When the RFs selected for stacking correspond to events with backazimuth and distance in small ranges, σ is computed by using the equation (A6). In order to get a variance estimate for a stacked receiver function computed from a RFs set with

backazimuth and distance varying in wide ranges, we tested intermediate values of σ^2 between σ_u^2 and $\min \sigma_k^2$ and found that

$$\sigma^2 = \frac{\sigma_u^2 + \min_k \sigma_k^2}{2} \quad (\text{A7})$$

provides a satisfactory agreement with the rms value, as shown in the Figure A1c. As a whole, this figure exhibits that, compared to the RFs standard deviations, the estimates for the stacked receiver functions are more scattered around the rms values, owing to the crude estimate of the correlation among the receiver functions selected for stacking.

Table 1. Events used in the RF analysis, each of them identified by its origin time (2-digits year, month, day,

hour and minute) . NRFs indicates the number of receiver functions selected for each event. Event data come from NEIC.

Event	NRFs	Latitude	Longitude	Depth	m_b	Region
				(km)		
9503311401	1	38.212	135.012	354	6.0	Sea of Japan
9504010550	2	52.264	159.043	30	5.9	Off east coast of Kamchatka Peninsula, Russia
9504040710	1	33.749	-38.623	10	5.2	Northern Mid-Atlantic Ridge
9504081913	1	52.171	159.046	38	5.6	Off east coast of Kamchatka Peninsula, Russia
9504140032	7	30.285	-103.347	17	5.6	Western Texas, United States
9504170714	8	33.763	-38.576	10	5.8	Northern Mid-Atlantic Ridge
9504172328	11	45.928	151.283	23	6.1	Kuril Islands, Russia
9504180523	2	45.829	151.444	33	5.7	Kuril Islands, Russia
9504190350	7	44.046	148.144	26	5.9	Kuril Islands, Russia
9504210002	2	11.973	125.688	27	5.4	Samar, Philippine Islands
9504210009	4	12.011	125.656	20	6.2	Samar, Philippine Islands
9504210030	5	11.925	125.564	17	6.3	Samar, Philippine Islands
9504210034	3	12.059	125.580	20	6.3	Samar, Philippine Islands
9504230255	9	51.334	179.714	16	6.2	Rat Islands, Aleutian Islands, United States
9504230508	7	12.390	125.396	24	6.1	Samar, Philippine Islands
9504232355	1	5.247	-72.476	33	5.3	Colombia
9504281630	9	44.072	148.004	28	6.5	Kuril Islands, Russia
9504281708	5	44.091	148.074	35	6.1	Kuril Islands, Russia
9504281744	1	-1.904	55.622	10	5.2	South Indian Ocean
9504290435	1	44.007	147.954	33	5.4	Kuril Islands, Russia
9504290943	4	11.853	125.982	15	5.5	Samar, Philippine Islands
9504291150	2	-1.315	28.605	10	5.1	Zaire
9505020354	3	43.302	147.325	49	5.6	Kuril Islands, Russia
9505020606	6	-3.792	-76.917	97	6.5	Northern Peru
9505021148	5	43.776	84.660	33	5.5	Northern Xinjiang, China

9505030838	7	12.824	125.098	34	6.2	Samar, Philippine Islands
9505060159	9	24.987	95.294	117	6.4	Myanmar
9505081740	2	43.856	148.342	21	5.7	East of Kuril Islands, Russia
9505150405	1	41.603	88.820	0	6.1	Southern Xinjiang, China
9505160335	3	36.455	70.893	186	5.7	Hindu Kush, Afghanistan, region
9505180006	6	-0.893	-21.996	12	6.2	Central Mid-Atlantic Ridge
9505181431	2	44.322	147.536	89	5.8	Kuril Islands, Russia
9505231001	6	43.655	141.736	17	5.5	Hokkaido, Japan, region
9505231548	1	51.138	-177.124	31	5.4	Andreanof Islands, Aleutian Islands, United States
9505241102	2	61.007	-150.119	41	5.3	Southern Alaska, United States
9505250459	1	43.926	147.331	51	5.6	Kuril Islands, Russia
9505250911	4	40.214	143.364	29	5.4	Off east coast of Honshu, Japan
9505260311	3	12.115	57.939	62	5.4	Owen Fracture Zone region
9505271303	10	52.629	142.827	11	6.7	Sakhalin Island, Russia
9505291021	2	52.686	142.850	33	5.3	Sakhalin Island, Russia
9505301615	1	43.341	146.908	54	5.1	Kuril Islands, Russia
9505311351	6	30.232	67.937	23	5.2	Pakistan
9506141111	4	12.128	-88.360	25	5.7	Off coast of central America
9506190057	1	44.090	150.415	33	5.3	East of Kuril Islands, Russia
9506220101	5	50.372	89.949	13	5.5	Tuva-Buryatia-Mongolia border region
9506250659	10	24.600	121.700	52	5.8	Taiwan
9506271009	9	18.835	-81.719	10	5.8	North of Honduras
9506290745	10	48.793	154.446	64	5.9	Kuril Islands, Russia
9506292302	9	51.961	103.099	11	5.6	Lake Baykal, Russia, region
9506301158	4	24.688	-110.228	10	5.9	Baja California, Mexico
9506301629	2	3.730	95.379	54	5.2	Off west coast of northern Sumatra, Indonesia
9507080542	4	39.678	143.352	11	5.9	Off east coast of Honshu, Japan
9507081715	8	53.578	-163.740	21	6.0	Unimak Island, Alaska, United States, region
9507092031	2	21.984	99.159	10	5.7	Myanmar-China border region
9507112146	5	21.966	99.196	12	6.1	Myanmar-China border region

Table 2. Values of the fixed parameters and ranges of variability for the other parameters, for 1-D models of the crust and upper-mantle structure consisting of 5 layers over an halfspace. In the first layer, the values of Q_P and Q_S are 675 and 300, respectively, if the selected minimum thickness is 5 km or higher.

	h (km)	ρ (kg/m ³)	V_S (km/s)	V_P/V_S	Q_P	Q_S
Layer 1	0.1 – 10	2600	0.5 – 3.6	1.6 – 3.0	100,675	25,300
Layer 2	0.1 – 10	2600	1.0 – 3.9	1.6 – 2.0	675	300
Layer 3	1 – 18	2600	2.0 – 4.5	1.6 – 1.9	1450	600
Layer 4	2 – 23	2600	2.8 – 4.8	1.6 – 1.9	1450	600
Layer 5	5 – 20	2600	3.2 – 5.0	1.6 – 1.9	1450	600
Halfspace		3300	3.5 – 5.0	1.7 – 1.9	1450	600

Table 3. Values of the fixed parameters and ranges of variability for the other parameters, for models of dipping structure in the near-surface crust for the station CA01. The strike angle is measured clockwise from the north; the dip angle is measured from the horizontal plane.

	h (km)	ρ (kg/m ³)	V_S (km/s)	V_P/V_S	Strike (degree)	Dip (degree)
Layer	0.1 – 4	2600	0.5 – 3.0	1.6 – 3.0	300 – 360	0 – 80
Halfspace		2600	1.5 – 3.5	1.6 – 2.5		

Table 4. Comparison between Moho depths obtained in this study and in the study by *Mele et al.* [2006].

Station	Moho depth (km)	
	This study	<i>Mele et al.</i> [2006]
CA00	24	22
CA01	20	22
CA02	25/30	29
CA03	30	33
CA04	32	31
CA05	28	41

CA06	37	47
CA07	36	42
CA08	36	39
CA09	41	40
CA10	29	40?
CA11	43/31	39
CA12	42	40
CA13	-	-
CA14	27	33

Figure Captions.

Figure 1. Location of the 15 broad band seismic stations (black triangles) installed along a transect crossing the central Apennines, from the Tyrrhenian coast to the Tremiti islands, in the Adriatic sea, both in map view (middle) and along a topographic profile (top). The main tectonic features of Italian region are represented in the bottom map (modified after *Cimini and Marchetti* [2006]), where the box highlights the study area.

Figure 2. Distribution of the 56 teleseisms used in this study.

Figure 3. Results from the analysis of the 39 RFs at station CA01. Radial receiver functions are plotted on the left (panel a) and tangential receiver functions are plotted on the right (panel b). All receiver functions are plotted to a common amplitude scale. The numbers between panels a and b are the backazimuth and epicentral distance, respectively, of the earthquake from the station. For the stacked RFs (the single-event traces used for stacking are not shown), the backazimuth (up) and epicentral distance (down) intervals are given on the left of panel a. The shaded area on both panels a and b, highlights the data segments used in the inversion for the shallow dipping structure, whose resulting synthetics RFs are drawn as red lines. RFs selected for the 1-D inversion are drawn with a thicker line in panel a, with backazimuth-epicentral distance attributes boldfaced. The synthetic RFs computed from the best-fit model obtained in the 1-D inversion are the dashed traces in panel d, super-imposed on the RFs selected for the 1-D inversion (solid traces). The S -wave velocity (solid line, top axis scale) and the V_P/V_S ratio (dashed line, bottom axis scale) are plotted versus depth (km) in panel c. The azimuthal plot inset in panel c shows the strike and the dip of the shallow dipping interface.

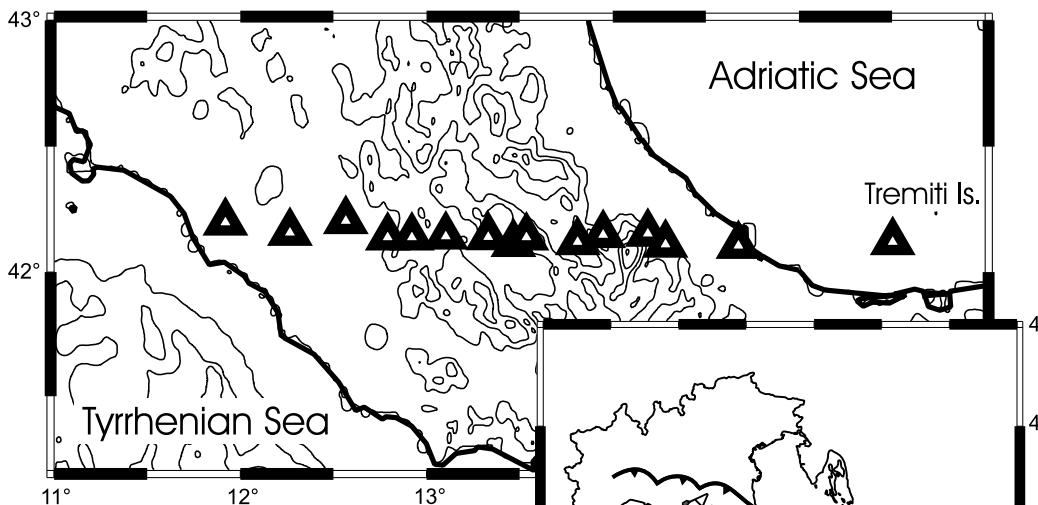
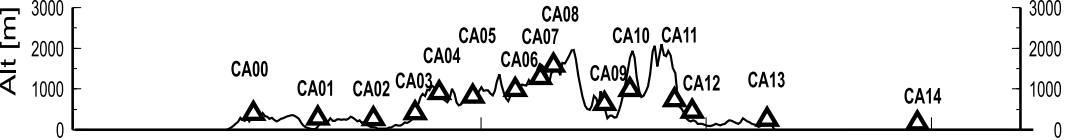
Figure 4. Comparison between the synthetic (dashed gray lines) and the observed traces (solid black lines), for representative receiver functions used in the inversion for the 1-D crust and upper mantle structure beneath each station of the CAP transect. For stations CA02 and CA11, the inversions for the eastern and western 1-D models are labeled with E and W, respectively.







Figure 5. Summary of the *S*-wave velocity models obtained in this study (red lines). On the top, the location of the recording sites (red triangles) on the topographic profile of the Apennines is shown. The blue dashed line highlights the crust-mantle boundary along the transect. The light red area evidences the low velocity zone found in the uppermost mantle on the Tyrrhenian side. The light blue area indicates the crustal volume, on the external front of the Apennines, where the attribution of the Moho to a definite interface is more uncertain. The yellow areas mark the presence of *S*-wave velocity inversion within the crust.

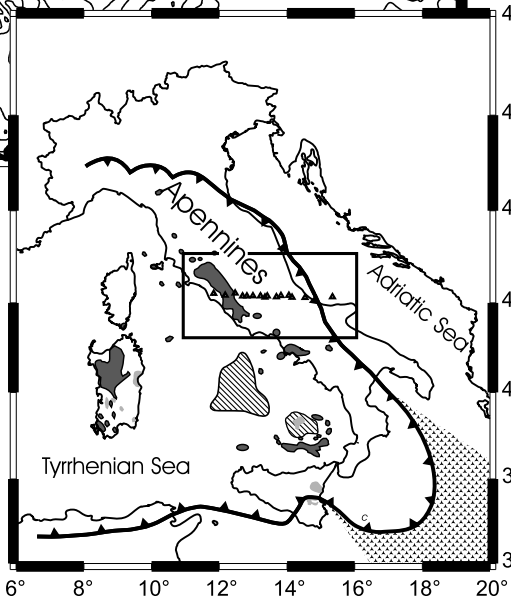
Figure 6. Summary of the MPPD functions for the average crustal V_P , V_S , and V_P/V_S , and for the Moho depth along the transect (from top to bottom). The MPPD functions for each quantity are plotted to a common amplitude scale. On the top, the location of the recording sites (red triangles) on the topographic profile of the Apennines is shown.

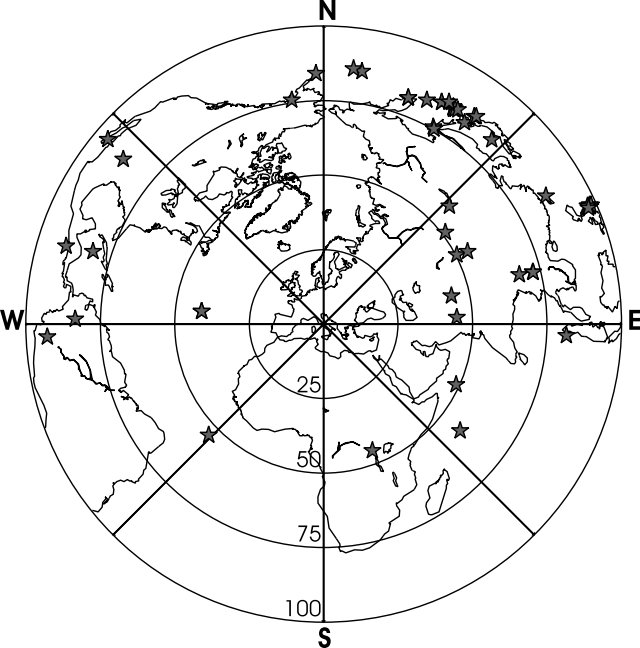
Figure A1. (a) Standard deviations of the radial RFs (backazimuth 25-36 degree, epicentral distance 75-86 degree) versus the events magnitude, for the station CA10; these RFs were stacked and the lines in the plot indicate, for the stacked receiver function, the rms value and the estimates of σ_u and σ (see the text for details). **(b)** Standard deviations of the radial RFs (backazimuth N73W – N75E, epicentral distance 73-98 degree) versus the events magnitude,

for the station CA03; black circles indicate the RF subset with more similar backazimuths (24-36 degree) and distances (76-86 degree); the two lines show the estimate of σ_u and the rms value for the stacked receiver function computed from the whole RF set. **(c)** Standard deviations versus the rms values, for the 248 selected radial receiver functions (small crosses) and for the stacked (radial) receiver functions; circles and triangles indicate RFs stacking respectively in small and large ranges of backazimuth and distance.



-  Seismic station
-  Orogenic, subduction related, volcanism
-  Anorogenic, extension related, volcanism
-  Present-day location of the convergent boundary
-  Newly formed oceanic crust
-  Mesozoic oceanic crust



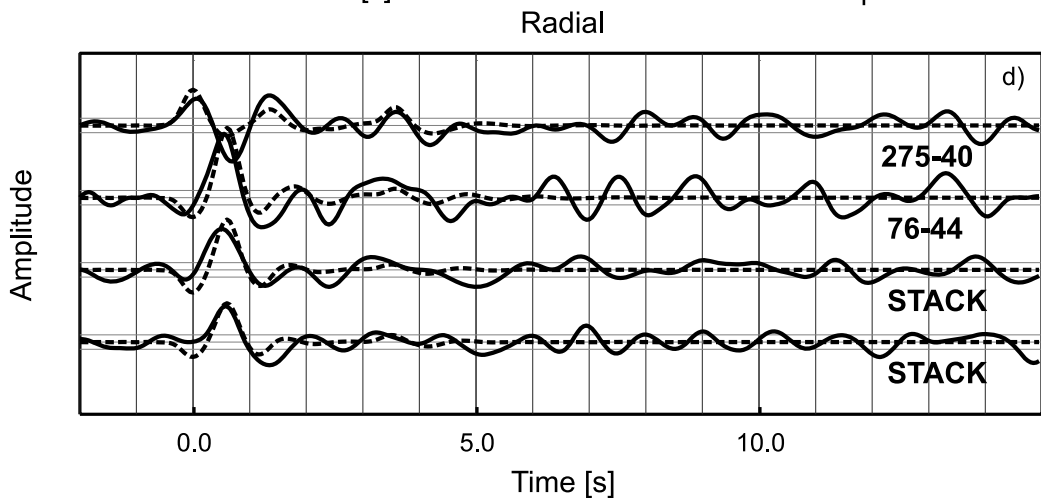
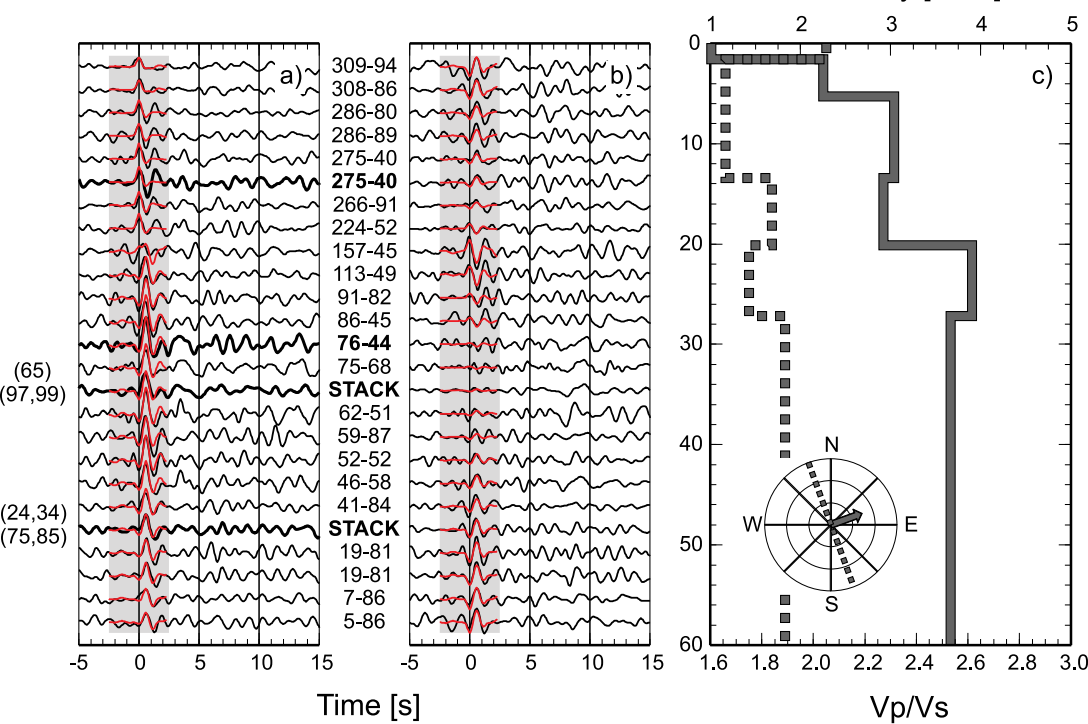


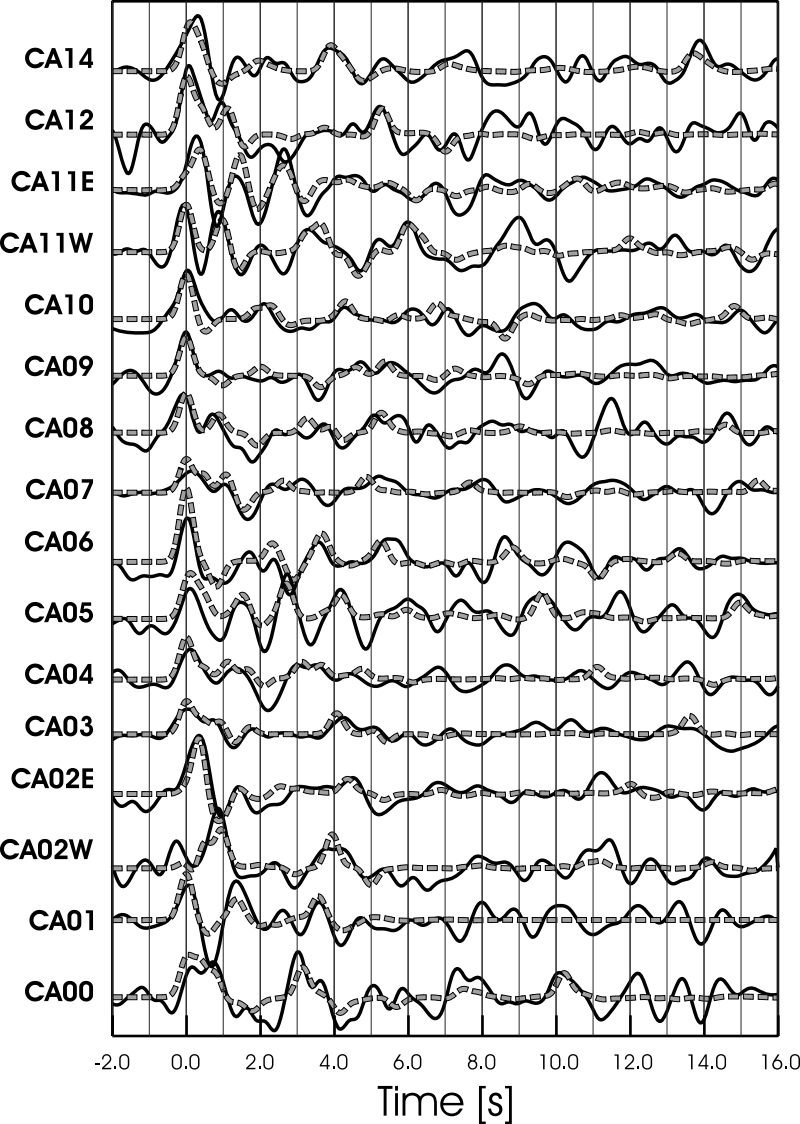
CA01

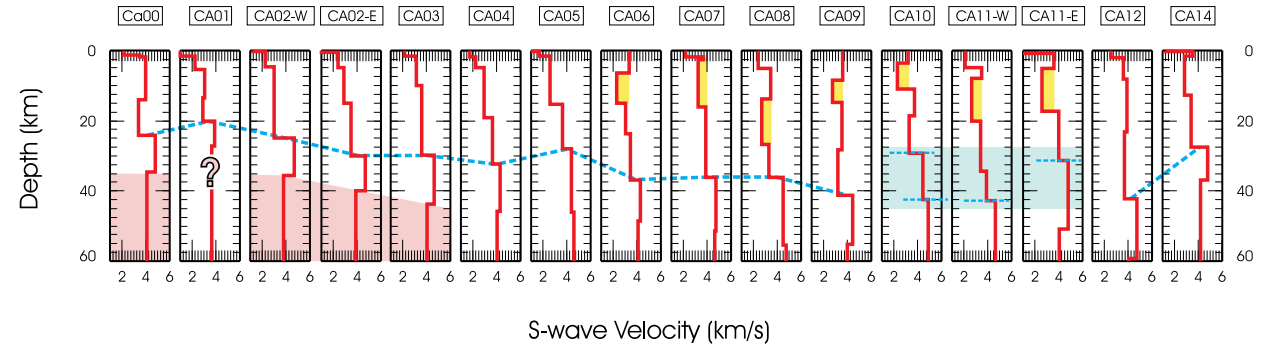
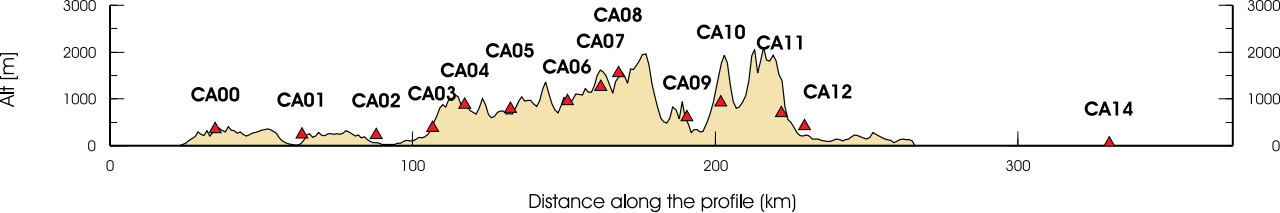
Radial

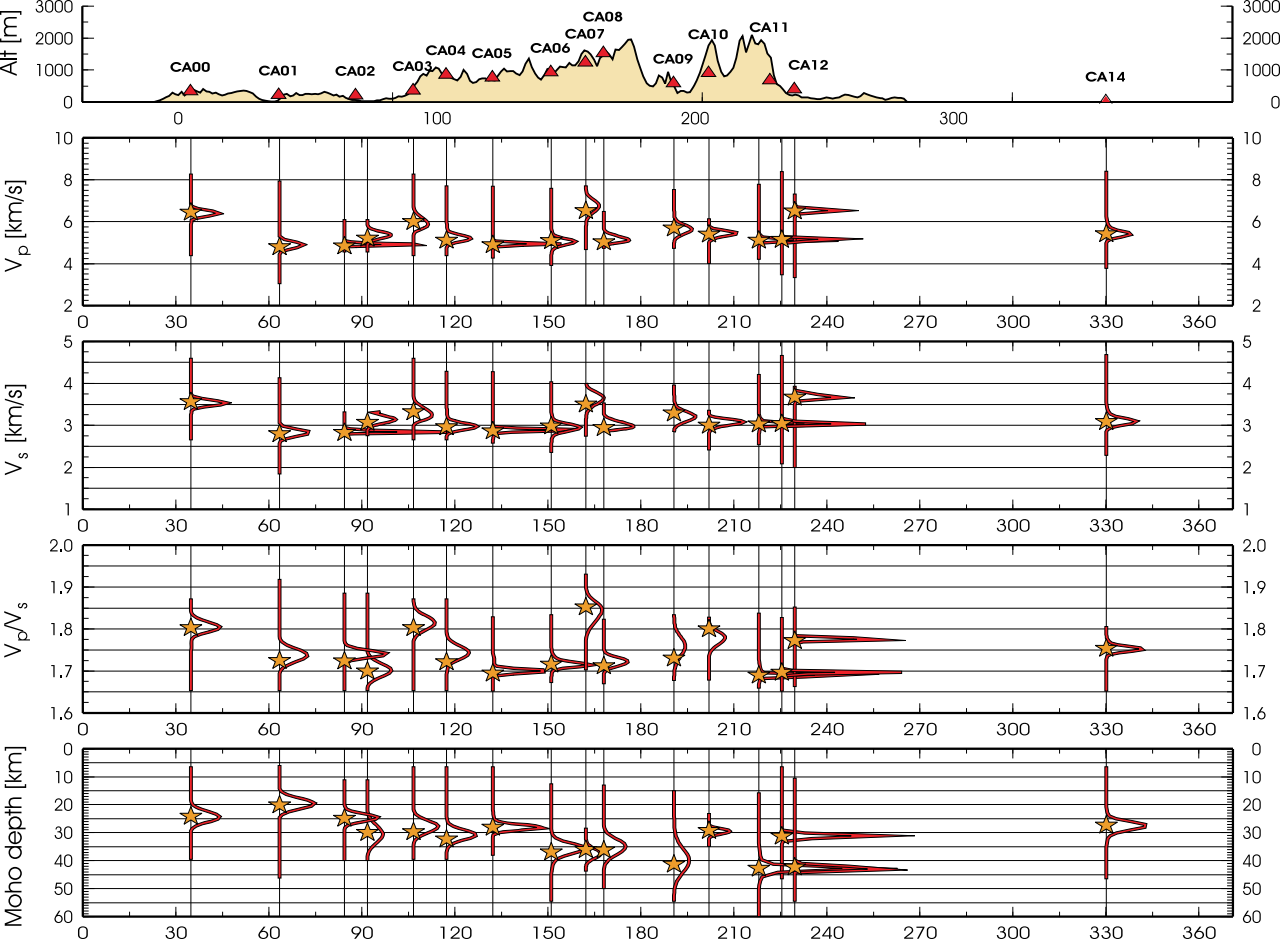
Transverse

S-velocity [km/s]

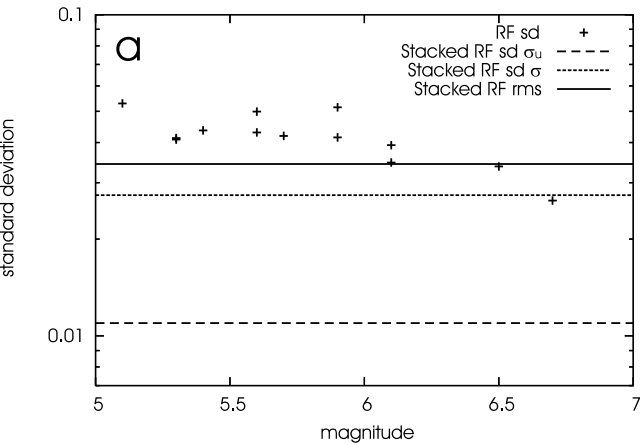








station CA10, component radial



station CA03, component radial

